Direct Observation of the Injection Dynamics of a Laser Wakefield Accelerator Using Few-Femtosecond Shadowgraphy

A Sävert, S.P.D Mangles, M Schnell, E Siminos, Jason M. Cole, M Leier, M Reuter, Matthew B. Schwab, M Möller, K Poder, et al.

Direct observation of the injection dynamics of a laser wakefield accelerator using few-femtosecond shadowgraphy

A. Sävert[1], S. P. D. Mangles[2], M. Schnell[1], E. Siminos[3], J. M. Cole[2], M. Leier[1], M. Reuter[4], M. B. Schwab[1], M. Möller[1], K. Poder[2], O. Jäckel[4], G. G. Paulus[1,4], C. Spielmann[1,4], S. Skupin[5], Z. Najmudin[2], and M. C. Kaluza[1,4]

[1] *Institut für Optik und Quantenelektronik, Abbe-Center of Photonics, Friedrich-Schiller-Universität, 07743 Jena, Germany*

[2] *The John Adams Institute for Accelerator Science, The Blackett Laboratory, Imperial College London, London SW7 2AZ, United Kingdom.*

[3] *Max Planck Institute for the Physics of Complex Systems, 01187 Dresden, Germany*

[4] *Helmholtz-Institut Jena, Friedrich-Schiller-Universität, 07743 Jena, Germany and*

[5] *Univ. Bordeaux - CNRS- CEA, Centre Lasers Intense et Applications, UMR 5107, 33405 Talence, France*

We present few-femtosecond shadowgraphic snapshots taken during the non-linear evolution of the plasma wave in a laser wakefield accelerator with transverse synchronized few-cycle probe pulses. These snapshots can be directly associated with the electron density distribution within the plasma wave and give quantitative information about its size and shape. Our results show that self-injection of electrons into the first plasma wave period is induced by a lengthening of the first plasma period. Three dimensional particle in cell simulations support our observations. Few-cycle transverse shadowgraphy opens a pristine view into the dynamics of plasma wakefield accelerators and can therefore be an invaluable tool in their optimization.

Laser-plasma accelerators operating in the 'bubble'-regime [1] can generate quasi-monoenergetic multi-giga-electronvolt electron beams [2, 3] with femtosecond duration [4, 5] and micrometer dimensions [6, 7]. These beams are produced by accelerating electrons in laser-driven plasma waves over centimeter distances only. Hence, they have the potential to be compact alternatives to conventional accelerators [8]. Laser wakefield accelerators (LWFA), driven by lasers with peak powers of 10-100 TW are already sources of high-energy electron bunches [9]. In such a LWFA, the intense pressure of the short driving laser pulse displaces plasma electrons from the stationary background ions. Due to the generated space charge fields the electrons start to oscillate and form a plasma wave in the wake of the laser pulse. This plasma wave co-propagates with the laser through the plasma at almost c, the speed of light. The wavelength of this plasma wave for low amplitudes is

$$\lambda_\mathrm{p} = 2\pi c\sqrt{\varepsilon_0 m_\mathrm{e}/(n_\mathrm{e}e^2)}, \qquad (1)$$

where e, m_e, and ε_0 are electron charge, mass and the vacuum permittivity, respectively and n_e is the electron number density of the plasma. When the plasma wave is driven to high amplitude, electrons from the background plasma can be self-injected into the wake and then accelerated, producing quasi-monoenergetic electron pulses. Since the first observation of these beams [10–12] significant progress has been made regarding achievable peak energy [3], beam stability [13] and the use of these beams to generate bright X-ray pulses for applications [14–16]. Up to now, most of our knowledge about the dynamics of the self-injection process has been derived from detailed numerical particle-in-cell simulations. These simulations show that processes such as self-focusing [17] and pulse compression [18] play a vital role in amplifying the laser pulse intensity prior to injection. However, experimental insight into the dynamics of these processes is extremely challenging due to the small spatial and temporal scales of a LWFA.

Since the plasma wave is associated with a variation in plasma density and therefore also in the plasma's refractive index, the wave can induce phase changes on an optical probe beam. In a co-propagating geometry the plasma wave can be detected by either time-domain interferometry (TDI) [19, 20], or in a single shot by frequency-domain holography (FDH) [21]. However, for these techniques to work the wave must not evolve significantly within the interaction distance. This can only be achieved in the quasi-linear regime of wakefield acceleration. In the non-linear or 'bubble'-regime, where almost all current LWFA experiments operate, feedback between the laser pulse and the plasma wave (i.e. the processes of self-focusing and pulse compression) leads to dramatic and rapid evolution of the plasma wave structure.

In addition, each period of the plasma wave consists of regions of very low electron density (the bubble) surrounded by high density (the bubble sheath). These steep density gradients lead to strong refraction of any co-propagating probe beam. Furthermore, to observe all details of the plasma wave oscillation and its evolution the use of diagnostics with a bandwidth capable of resolving temporal structures much smaller than λ_p/c is essential. Thus a transverse probing geometry with a probe pulse having a duration significantly shorter than the plasma wave period is required.

In the present study, the JETI-laser system at the Institut für Optik und Quantenelektronik in Jena, Germany produced pump pulses to drive a LWFA. JETI delivers pulses of 750 mJ energy and 35 fs duration at a central wavelength of $\lambda_\mathrm{L} = 810$ nm. The pulses were

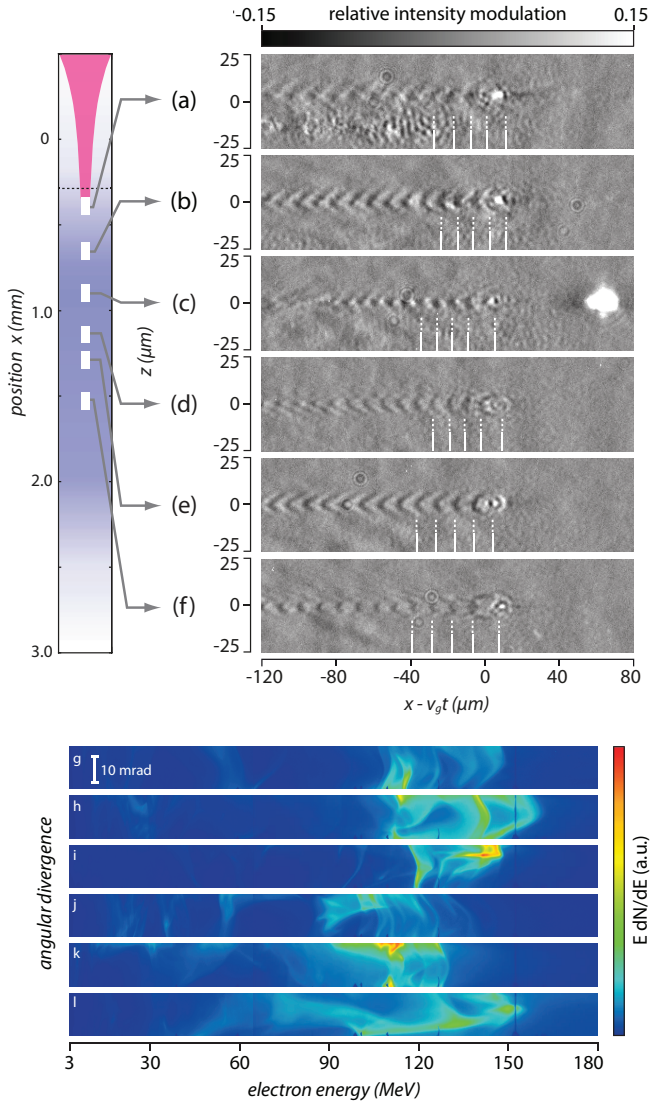

FIG. 1. Evolution of the laser-wakefield. Left: electron density profile of the gas jet and focus position (dashed line). Experimental shadowgrams at various positions (a-f) in the plasma at a background electron density of $n_e = 1.65 \times 10^{19} \mathrm{cm}^{-3}$. Energy in the electron beam per MeV and spatially resolved in the vertical coordinate corresponding to the delay steps above (g-l, same order).

focused by an $f/13$ off-axis parabolic mirror to an elliptical focal spot with dimensions (FWHM) $12.8\mu\mathrm{m} \times 8.9\mu\mathrm{m}$ containing 27% of the energy, resulting in peak intensities of $I_\mathrm{L} = 6 \times 10^{18}\,\mathrm{W/cm^2}$ (corresponding to a peak normalized vector potential of $a_0 = 8.55 \times 10^{-10} \lambda_L(\mu\mathrm{m}) \cdot \sqrt{\mathrm{I_L(W/cm^2)}} \approx 1.7$). A supersonic helium gas jet was used, generating a plasma with electron density n_e in the range of $(0.5 \ldots 2.5) \times 10^{19}\,\mathrm{cm}^{-3}$. Electrons accelerated during the interaction could either be detected using a high-resolution magnetic spectrometer or a scintillating screen in the electrons' path. A small fraction of the laser was split from the main pulse, spectrally broadened in a hollow-core fiber filled with argon gas to support a transform limited pulse duration of $\tau_\mathrm{FL} = 4.4\,\mathrm{fs}$. Using dispersive mirrors and glass wedges to optimize dispersion, probe pulses with duration as short as $\tau_\mathrm{probe} = (5.9 \pm 0.4)\,\mathrm{fs}$ were created [22]. These synchronized, few-cycle probe pulses were used to backlight the LWFA perpendicularly to the pump-pulse direction. A high-resolution imaging system produced shadowgraphic images with micrometer resolution on a CCD camera. To reduce modulations induced by the probe pulse's beam profile, the relative intensity modulation was plotted using $I_\mathrm{norm} = (I - I_0)/I_0$, with I being the pixel value at each individual position and I_0 the value derived from a low order spline fit in the horizontal direction.

By varying the delay between pump and probe pulse, different stages of the plasma wave's evolution were recorded on subsequent shots at the threshold density for self injection. The snapshots shown in Fig. 1 are representative for each evolutionary stage during the acceleration process. Images were selected exhibiting similar electron spectra with a narrow energy spread between 100 MeV and 150 MeV as shown in Fig. 1(g-l) and having a good image quality, i.e. a high contrast. The latter was influenced by the jitter in probe pulse duration and pointing fluctuations of the pump pulse which shifts the image out of focus. As the pump pulse propagates up the initial density ramp, the regions of high and low electron density gradient (dark and light regions in the image) are approximately equal in length, indicating a linear plasma wave, Fig. 1(a). In this region some scattered radiation is visible, emanating from the pump pulse. We attribute this to Raman side scattering due to asymmetries in the initial pump pulse. The transverse extent of the plasma wave reduces and the amplitude of the wave increases, Fig. 1(b), due to plasma-induced self-focussing and pulse compression of the pump pulse. A significant increase of curvature of the plasma-wave train and, in particular, in the lengthening of the first plasma period, Fig. 1(c) is apparent. Just ahead of the region where this lengthening starts we observe bright emission from the plasma. Spectrally resolved measurements reveal its broadband spectrum which is consistent with 'wavebreaking radiation' [23]. This emission is a direct signature of the point of self-injection in the experiment. Further propagation enhances the density gradient at the front of the bubble which now appears in the shadowgrams at the beginning of the wave train with a curvature in the opposite direction. After wavebreaking, the wave becomes highly non-linear, as indicated by the additional reversal in the direction of curvature of the trailing wave periods in the shadowgrams, Fig. 1(d) to 1(f). These features are closely linked to the process of transverse wavebreaking [24].

Our ability to take time-resolved snapshots of the interaction allows us to show for the first time that the

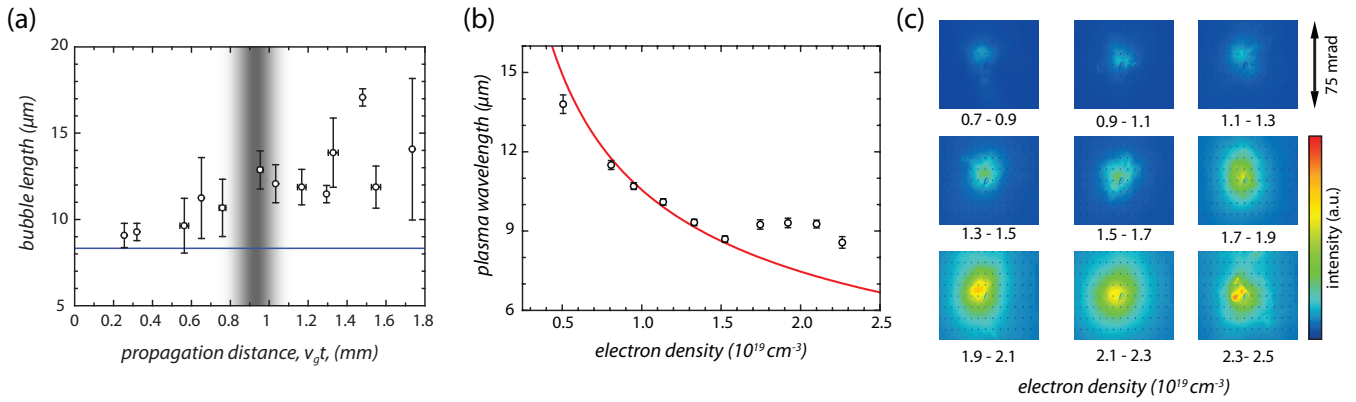

FIG. 2. Evolution of 1^{st} and length of 2^{nd} plasma wave period and electron beam profiles for different densities. (a) Length of the first plasma period (bubble) as a function of propagation distance $v_g t$ taken from the shadowgrams [error bars represent combination of uncertainty in determining the bubble length ($\pm 0.5\,\mu$m) in a single shot reduced by $\sqrt{N}$ where repeat shots are available]. Blue horizontal line is the expected plasma wavelength for $n_e = 1.65 \times 10^{19}\,\mathrm{cm}^{-3}$. Between $v_g t = 0.86$ and 1.0 mm (grey shaded area) wavebreaking radiation was frequently detected. (b) Wavelength of second plasma period versus n_e at a fixed position $v_g t = 1.0$ mm. Open circles represent measured and averaged data points with the standard error of the mean and red line is according to Eq. (1). (c) Electron beam profiles for different plasma densities averaged over 40-180 shots.

dynamic process of bubble lengthening is intimately tied to self-injection. To emphasize the importance of bubble expansion on injection, we plot in Fig. 2(a) the evolution of the plasma wave's first period. Early in the interaction the length of the first period has already increased as compared to a linear excitation. The length of the bubble is increasing up to the point of wavebreaking, which is characterized by a bright emission of radiation. During a single interaction, this radiation is emitted from a distinct spot on the optical axis. Its longitudinal position varies slightly from shot to shot around $(930\pm67)\,\mu$m. Afterwards the shape of the plasma wave varies from shot to shot due to the strongly non-linear behaviour. Depending on the laser parameters, this can lead to complete wavebreaking and the formation of a single bubble or to the merging of the first two plasma wave periods.

We also measured the length of the second wave period, shown in Fig. 2(b), as a function of density at a fixed position in the plasma ($v_g t = 1.0$ mm). These measurements were made sufficiently far into the gas jet to ensure that it was in the uniform density plateau. At low densities, the length is well matched to Eq. (1), but at high densities, λ_p is significantly longer. The density at which this transition occurs corresponds to the density where we start to observe significant charge in the accelerated electron beam, see Fig. 2(c), and to the self-injection threshold predicted in Ref [25]. As n_e is increased beyond $1.7 \times 10^{19}\,\mathrm{cm}^{-3}$, the wavelength observed at this fixed position remains approximately constant, rather than decreasing $\sim n_e^{-1/2}$ as expected. This lengthening is a direct consequence of the relativistic mass increase of the electrons in the plasma wave and of its nonlinear evolution that affects all the periods of the wave train.

In addition, three dimensional particle in cell (3D-PIC) simulations were performed with the code EPOCH [26]. A laser pulse with $\tau_L = 36$ fs and $\lambda_L = 810$ nm was focused to a spot size of $18.8\,\mu$m (FWHM), $300\,\mu$m into a plasma density profile that matched the experimentally measured one (with a peak density $n_e = 1.7 \times 10^{19}\,\mathrm{cm}^{-3}$). In order to take into account imperfections in the experimental focal spot we set the maximum intensity of the laser pulse to $I_0 = 2.5 \times 10^{18}\,\mathrm{W/cm}^2$, leading to similar energies within the focal spot FWHM in experiments and simulation [27]. The computational domain was a 'sliding window' of size $150 \times 70 \times 70\,\mu\mathrm{m}^3$ moving at c. We used $2700 \times 525 \times 525$ cells with two electrons per cell and a stationary ion background. A 6^{th} order finite-difference-time-domain scheme was employed, together with 5^{th} order particle weighting. Probe propagation has also been fully simulated in 3D with EPOCH. At different times in the driver pulse propagation the moving window was stopped and a probe pulse was injected from the side of the box, propagating along the negative y direction, perpendicularly to the pump pulse direction. The probe pulse had a central wavelength $\lambda_{probe} = 750$ nm, a Fourier limited duration of 4.4 fs and a positive linear chirp that increased its duration to 12 fs for a best match to the experimental images. We allowed the probe pulse to propagate past the wakefield structure, until approximately $y = -15\,\mu$m. Subsequently, propagation in vacuum was assumed and modeled in Fourier space including the imaging system aperture, sensor sensitivity and image plane position. To adjust for the latter, we propagated the probe pulse backwards and recorded the time-averaged Poynting flux through the object plane, which in the images presented here was taken to be at $y = 0$. The comparison of density maps and PIC generated shad-

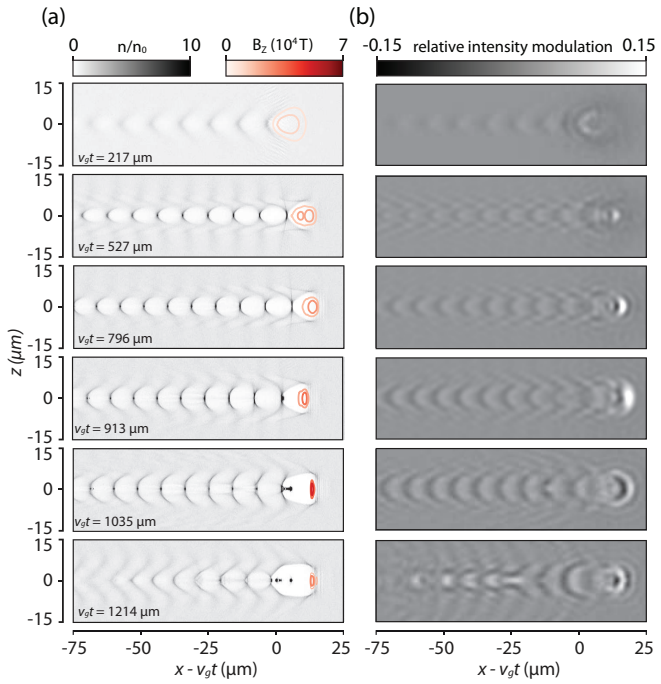

FIG. 3. (a) Electron density maps (gray) from the simulations at various positions and contours of the envelope of pump magnetic field B_z (red) corresponding to 50% and 75% of the maximum value. (b) Shadowgrams simulated from the simulations in Fig. 3(a).

owgrams in Fig. 3 verifies that shadowgrams capture local variations in plasma density and allows a direct interpretation of the experimental shadowgrams. Particularly interesting is the fact that the injected electron bunch neither appears in the simulated nor the experimental shadowgrams in Fig. 1. This is caused by the reduction of local plasma frequency due to the relativistic mass correction to the index of refraction $\eta = \left[1 - \omega_p^2/(\gamma\,\omega_{\mathrm{probe}}^2)\right]^{1/2}$, where ω_{probe} is the probe frequency, $\gamma = \left(1 - v^2/c^2\right)^{-1/2}$, and v is the averaged electron velocity. These simulated probe images confirm that few-femtosecond shadowgraphy provides quantitative information about the plasma wave including the plasma wave length, curvature and number of trailing periods.

The length of the first plasma period, i.e. the bubble, as determined by the density maps from the PIC simulations at various positions during the evolution is shown in Fig. 4 together with the maximum amplitude of the pump pulse's Poynting vector, which is associated with the local intensity, and the total injected charge with energy above 20 MeV from the PIC simulations. The intensity increase due to pump pulse compression and self-focusing [see also Fig. 3(a)] is slow until approximately $v_g t = 800\,\mu$m. Until that point the bubble length grows from $1.2\,\lambda_p$ to $1.5\,\lambda_p$. After $v_g t = 800\,\mu$m a phase of rapid intensity amplification begins, accompanied by bubble expansion and injection around $v_g t = 930\,\mu$m. At this stage, there is no charge injected and so the bubble expansion is not due to beam-loading but due to intensity amplification of the pump pulse; $\lambda_p^* \approx \lambda_p(1 + a_0^2/2)^{1/4}$ [28]. In the PIC simulation significant charge is only injected into the wake (around $v_g t = 930\,\mu$m) after the length of the bubble has started to increase as also observed previously in simulations [10, 29, 30]. This intensity amplification manifests itself in an increased visibility of the front of the bubble in the simulation shadowgrams, Fig. 3(b), which can also be observed in the experimental data, Fig. 1(e-f). After $v_g t = 1000\,\mu$m, the intensity decreases, while the length of the bubble keeps increasing due to beam-loading. At approximately $v_g t = 1300\,\mu$m, the simulations show a merging of the first two periods of the wake. The 3D simulations support the experimental observation that self-injection in the laser wakefield accelerator only occurs after the bubble length significantly increases, and that this lengthening is due to the increase in pump intensity induced by self-focussing and pulse compression.

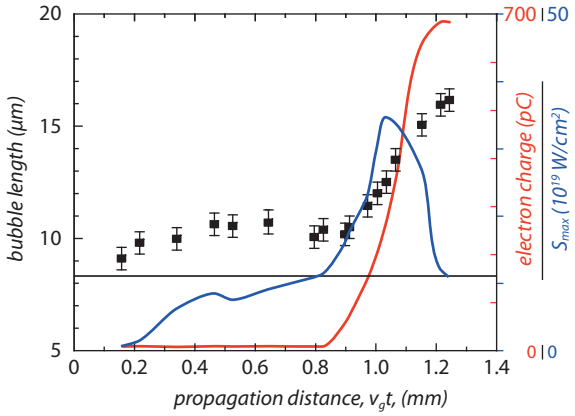

FIG. 4. Bubble length derived from density maps (black squares) and injected charge with energy larger than 20 MeV (red line) from the PIC simulation and maximum instantaneous value S_{max} of the Poynting vector magnitude (blue line) from the PIC simulations.

Applying our approach to visualize the full non-linear evolution of the plasma wave allows the acceleration process to be studied with unprecedented precision. As well as providing greater understanding of acceleration in the bubble-regime, our technique can easily be adopted to more complex acceleration geometries, e.g. staging [13], or for beam-driven acceleration [31–33]. Furthermore, increasing the probe pulse's wavelength while keeping a few-cycle duration will increase the sensitivity of our technique to probe low-density plasmas while keeping the relative resolution. Such low plasma densities are essential for high-energy plasma-electron acceleration scenar-

ios. As laser wakefield accelerators are widely expected to become useful sources of ultra short radiation [34], the increased level of understanding of plasma wave evolution and injection that can be gleaned from few-femtosecond shadowgraphy and the improvements in beam properties that will result from this technique are therefore likely to have a large impact on biomedical imaging and ultrafast condensed-matter study.

We thank B. Beleites, W. Ziegler, and F. Ronneberger for running the JETI-laser system. E.S. and S.S. would like to thank V. T. Tikhonchuk for helpful discussions. This study was supported by DFG (grants TR18 A12, B9 and KA 2869/2-1), BMBF (contracts 05K10SJ2 and 03ZIK052), European Regional Development Fund (EFRE), STFC (ST/J002062/1) and EPSRC (EP/H00601X/1). The collaboration was funded by LASERLAB-EUROPE (grant agreement n° 284464, EC's Seventh Framework Programme). EPOCH was developed under UK EPSRC grants EP/G054940/1, EP/G055165/1 and EP/G056803/1.

[1] A. Pukhov and J. Meyer-ter-Vehn, Appl. Phys. B **74**, 355 (2002).
[2] W. P. Leemans *et al.*, Nature Phys. **2**, 696 (2006).
[3] X. Wang *et al.*, Nature Commun. **4**, 2988 (2013).
[4] O. Lundh *et al.*, Nature Phys. **7**, 219 (2011).
[5] A. Buck *et al.*, Nature Phys. **7**, 543 (2011).
[6] M. Schnell *et al.*, Phys. Rev. Lett. **108**, 075001 (2012).
[7] G. R. Plateau *et al.*, Phys. Rev. Lett. **109**, 064802 (2012).
[8] S. M. Hooker, Nature Photon. **7**, 775 (2013).
[9] S. Kneip *et al.*, Phys. Rev. Lett.**103**, 035002 (2009).
[10] S. P. D. Mangles *et al.*, Nature **431**, 535 (2004).
[11] C. G. R. Geddes *et al.*, Nature **431**, 538 (2004).
[12] J. Faure *et al.*, Nature **431**, 541 (2004).
[13] A. J. Gonsalves *et al.*, Nature Phys. **7**, 862 (2011).
[14] A. Rousse *et al.*, Phys. Rev. Lett. **93**, 135005 (2004).
[15] S. Kneip *et al.*, Nature Phys. **6**, 980 (2010).
[16] S. M. Powers *et al.*, Nature Photon. **8**, 28 (2014).
[17] A. G. R. Thomas *et al.*, Phys. Rev. Lett. **98**, 095004 (2007).
[18] J. Faure *et al.*, Phys. Rev. Lett. **95**, 205003 (2005).
[19] J. R. Marques *et al.*, Phys. Rev. Lett. **76**, 3566 (1996).
[20] C. W. Siders *et al.*, Phys. Rev. Lett. **76**, 3570 (1996).
[21] N. H. Matlis, *et al.*, Nature Phys. **2**, 749 (2006).
[22] M. B. Schwab *et al.*, Appl. Phys. Lett. **103**, 191118 (2013).
[23] A. G. R. Thomas *et al.*, Phys. Rev. Lett. **98**, 054802 (2007).
[24] S. V. Bulanov *et al.*, Phys. Rev. Lett. **78**, 4205 (1997).
[25] S. P. D. Mangles *et al.*, Phys. Rev. ST Accel. Beams **15**, 011302 (2012).
[26] http://ccpforge.cse.rl.ac.uk/gf/project/epoch
[27] G. Genoud, *et al.*, Phys. Plasmas, **20** 064501 (2013).
[28] W. Lu *et al.*, Phys. Rev. ST Accel. Beams **10**, 061301 (2007).
[29] S. Bulanov *et al.*, Phys. Rev. E **58**, R5257 (1998).
[30] S. Kalmykov *et al.*, Phys. Rev. Lett. **103**, 135004 (2009).
[31] I. Blumenfeld *et al.*, Nature **445**, 741 (2007).
[32] A. Caldwell *et al.*, Nature Phys. **5**, 363 (2009).
[33] M. Litos *et al.*, Nature **515**, 92 (2014).
[34] F. Albert, *et al.*, Plasma Phys. Control. Fusion **56**, 084015 (2014).